Supporting information for: Characterization of Few-Layer 1T′ $MoTe_2$ by Polarization-Resolved Second Harmonic Generation and Raman Scattering

Ryan Beams,[†] Luiz Gustavo Cançado,[‡] Sergiy Krylyuk,[†,¶] Irina Kalish,[†] Berç Kalanyan,[†] Arunima K. Singh,[†] Kamal Choudhary,[†] Alina Bruma,[†] Patrick M. Vora,[§] Francesca Tavazza,[†] Albert V. Davydov,[†] and Stephan J. Stranick*[,†]

†*Material Measurement Laboratory, National Institute of Standards and Technology, Gaithersburg, MD 20899, U.S.A.*

‡*Departamento de Física, Universidade Federal de Minas Gerais, Belo Horizonte, MG 30123-970, Brazil*

¶*Theiss Research, La Jolla, CA, 92037 USA*

§*Department of Physics and Astronomy, George Mason University, VA, USA*

E-mail: stephan.stranick@nist.gov

Character tables

Table S1: Character table for the C_{2h} point group, corresponding to the N-layer 1T′ $MoTe_2$ with N odd (C_{2h}^2, or $P2_1/m$ space group symmetry). E is the identity, C_{2y} is a two-fold rotation axis along y, σ_{xz} is an horizontal plane mirror (parallel to xz), and i is the inversion. These symmetry elements, as well as the Cartesian coordinates are defined in Figs. 1 a,b. The first column indicates the irreducible representations, and the last column gives the corresponding basis functions.[S1]

	E	C_{2y}	σ_{xz}	i	
A_g	1	1	1	1	x^2, y^2, z^2, xz
B_g	1	1	-1	-1	y
A_u	1	-1	-1	1	xy, yz
B_u	1	-1	1	-1	x, z

Table S2: Character table for the C_s point group, corresponding to the N-layer 1T′ $MoTe_2$ with N even (C_s^1, or Pm space group symmetry). Same geometrical definitions as for Table S1 apply.[S1]

	E	σ_{xz}	
A'	1	1	x, z, x^2, y^2, z^2, xz
A''	1	-1	y, xy, yz

Tables S1 and S2 using the coordinate system defined in Figure 1 of the main text, which is rotated compared to many reference books. Similarly, the Raman tensors in Eqs.6 and 7 are rotated to keep the coordinate system consistent throughout the work.

Density-functional theory simulations of Raman modes

Table S3 shows the lattice constants, a, b and β, and symmetry of $1T'$-$MoTe_2$ as a function of number of layers. The lattice parameters change minimally as the number of layers increases with the most noticeable change in the b-lattice parameter, the b-lattice parameter of 1-layer $1T'$-$MoTe_2$ being 1.36% smaller than that of the bulk $1T'$-$MoTe_2$. The lattice parameters computed from the DFT simulations have an excellent agreement with the experimentally

measured values, differing by $< 2\%$. The 1-layer, 3-layer and bulk structures are found to have a C_{2h}^2 space group and the 2-layer and 4-layer structures have the C_s^1 space group.

Table S3: Lattice vectors, a, b and c in Å, angle β in ° and the symmetry of of N-layer $1T'$-$MoTe_2$ as computed from DFT simulations.

	a	b	β	Symmetry
Bulk	6.361	3.526	92.18	C_{2h}^1 ($P2_1/m$, #11)
	c = 14.137			
1-layer	6.356	3.478	92.15	C_{2h}^1 ($P2_1/m$, #11)
2-layer	6.352	3.496	92.15	C_s^1 (Pm, #6)
3-layer	6.353	3.504	92.15	C_{2h}^1 ($P2_1/m$, #11)
4-layer	6.354	3.511	92.15	C_s^1 (Pm, #6)

Substrate effects and experimental validation using MoS_2

The second order susceptibility, $\chi^{(2)}$, of 1T′ $MoTe_2$ was calibrated by measuring monolayer MoS_2 under the same measurement conditions. Since the $MoTe_2$ samples were prepared on an SiO_2/Si substrate, there was an additional contribution to the SHG signal due to the cavity created by the SiO_2/Si. While this term has been shown to be negligible,[S2–S4] we prepared monolayer MoS_2 samples on glass and SiO_2/Si to experimentally measure the cavity contribution. In Figure S1 the top and bottom rows show the samples on glass and SiO_2/Si, respectively. Figure S1 a,b show the white light images of the MoS_2 samples with the monolayer regions labeled. The single layer regions were verified using photoluminescence (PL) and Raman spectroscopy. The PL of the monolayer regions with the A and B excitons labeled are shown in Figure S1 b,c. Figure S1 d,e shows the Raman spectra. The PL[S5] and Raman[S5,S6] confirmed that the regions of interest are monolayer. Finally, SHG images on the same intensity scale of both regions are shown in Figure S1 f,g with linecuts shown in the insets. In this case no analyzer was used to remove the polarization dependence. These images show that the SHG signals are equivalent within our measurement accuracy. Therefore the signal enhancement from the cavity is negligible, as expected. Finally the SHG polar maps of the monolayer flake with the polarizer and analyzer parallel (black) and

crossed (red) are shown in Figure S1.

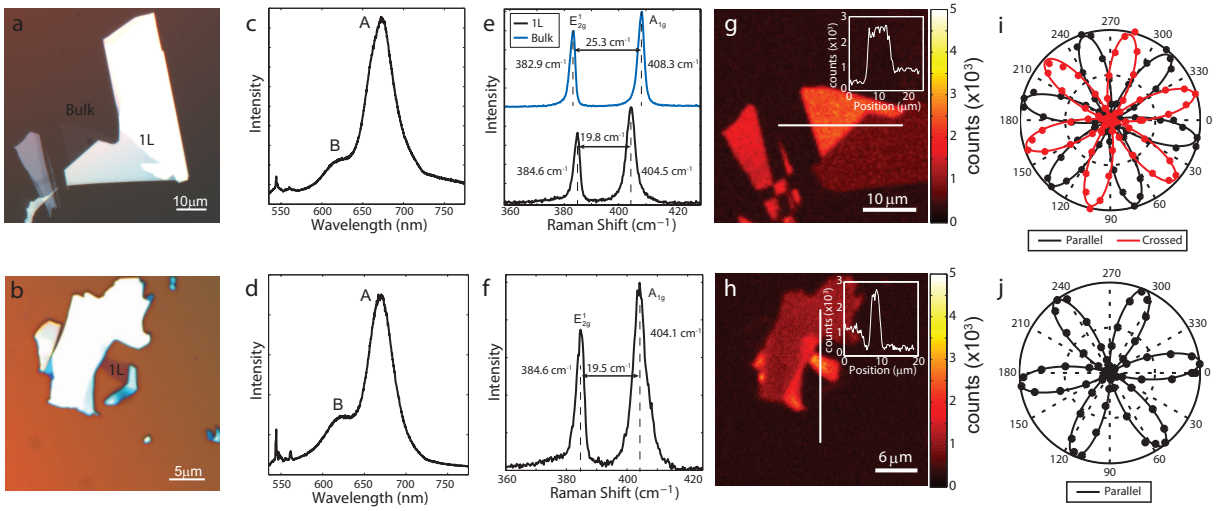

Figure S1: Characterization of monolayer MoS_2 samples. The top (bottom) row is a sample exfoliated on glass (SiO_2/Si). (a),(b) White light images of the MoS_2 samples with the monolayer sections labeled. (b),(c) Photoluminescence spectra of the two monolayer samples. (d),(e) Raman spectra of the two monolayer samples. (g),(h) SHG images of the two samples on the same intensity scale. (i) SHG polar maps of the monolayer flake with the polarizer and analyzer parallel (black) and crossed (red).

Laser damage and Raman measurement of additional flake

Figure S2 shows the Raman polarization dependence of the $N = 4$ sample from Figure 3 in the main text. The top set of plots is the raw data and a significant signal decrease is observed due to laser damage. The open circle data points were used for the damage plots in Figure S4. These points show the exponential decrease in the signal level. In order to plot the modes with A_g on the same scale as the modes with B_g symmetry, the first maximum for the A_g modes was scaled by the fractional signal decrease of the B_g by that time in the acquisition. The lower set of plots was corrected by dividing each data point by the fit from the exponential decay. After this correction, the Raman polarization equations from the main text were used to fit this data. There are a few differences from the polarization dependence for the $N = 12$ region in the main text. First, only one Lorentzian was used

to fit the peak at ≈260 cm^{-1} since a high energy tail was not observed. Also, an additional Lorentzian centered at 156 cm^{-1} was used to fit the laser damage induced broad shoulder that developed on the ≈160 cm^{-1} peak. The amplitude of that peak increases during the polarization measurements as expected for laser damage. From the Raman measurements, θ_0 = -54°, which is in excellent agreement with the SHG images once the sample mounting angle is taken into account (see below).

The final aspect of the Raman measurements that we will discuss is the low damage threshold for this material. For the 2H phase, oxidation[S7] and laser induced phase changes have been reported;[S8] however, damage and oxidation have not been reported for 1T′. Our sample was stored in an N_2 environment except for during measurements to try to minimize oxidation. As mentioned in the main text, the samples were measured using 350 μW with a 0.75NA objective, which is between a factor 5 to 10 lower power than is commonly used for other TMDs and graphene. This power was chosen because higher powers showed laser damage over several hour exposures for bulk crystals, which manifested as a decrease in the Raman signal. At 350 μW no appreciable laser damage was observed for the $N = 12$ region, as can be seen by the constant amplitudes in Figure 4 of the main text. However, for the $N = 4$ and $N = 3$ regions an exponential decrease in the Raman signal was observed, as shown in the raw data in Figure S3.

Figure S4 a,b shows the initial Raman spectra of the $N = 4$ region and after 80 min of laser exposure, both of them on the same intensity scale. The Raman signal decreased for all the modes and a high and low energy shoulder developed on the mode at ≈ 80 cm^{-1} and ≈ 160 cm^{-1}, respectively. To better illustrate the shoulders, a difference spectra of Figure S4 a and b after re-scaling is shown in blue. The absence of Raman peaks from 300-500 cm^{-1} suggests that the shoulders are not caused by TeO_2[S9] or MoO_2.[S10,S11] MoO_3 has peaks at ≈ 89 cm^{-1} and ≈ 160 cm^{-1} in agreement with the spectral location of the shoulders. However, MoO_3 also has a peak at ≈ 285 cm^{-1} and the amplitude of the slight peak at that

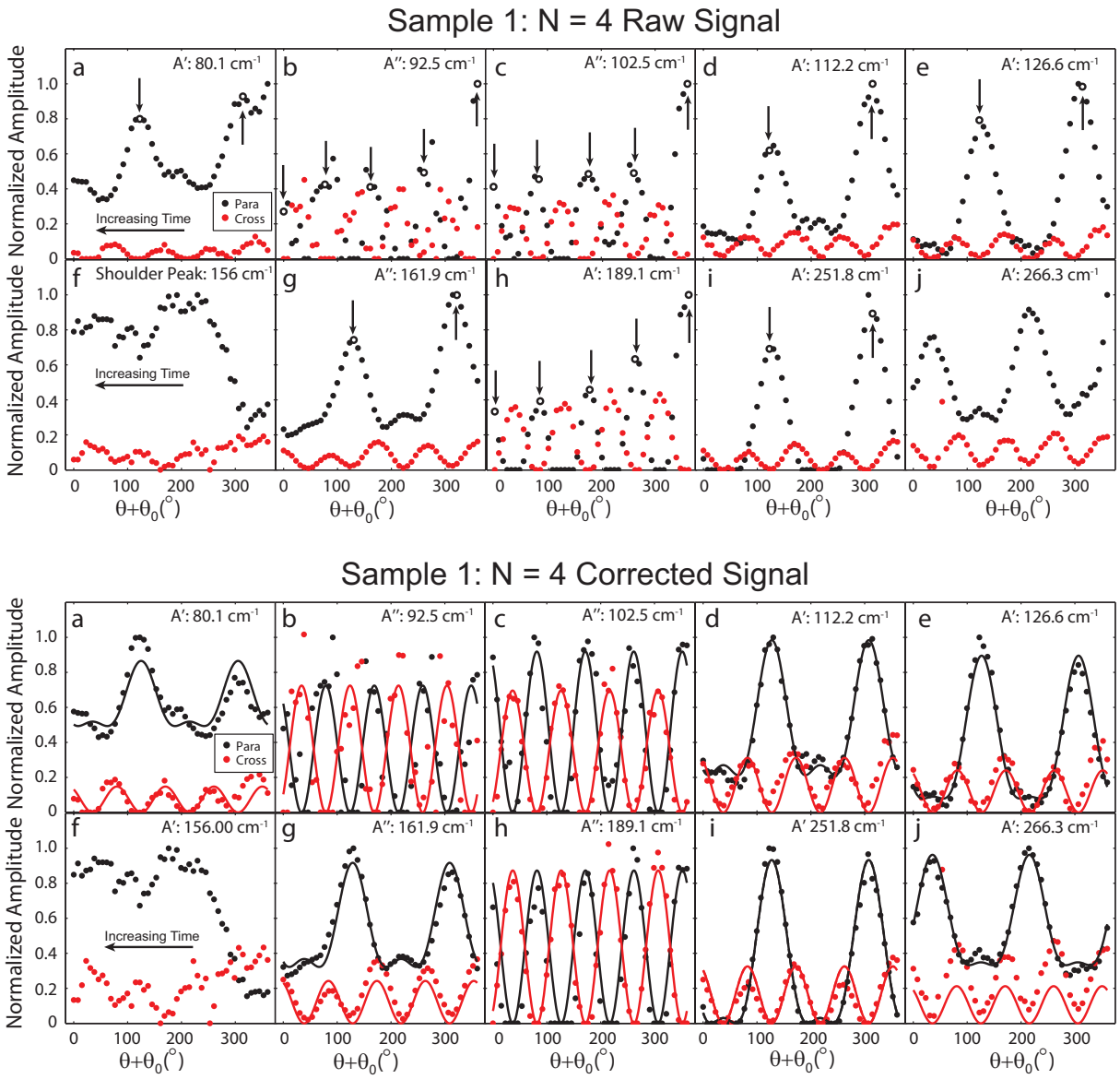

Figure S2: Normalized Raman amplitudes for parallel (red) and crossed (black) polarizations for the $N = 4$ region for Sample 1. The symmetry and position for each mode are labeled. The top set is the raw data and the bottom set is after correcting for the signal decrease. The fits using the complex Raman tensors (solid lines) are shown.

spectral location does not increase. Amorphous tellurium also has peaks at approximately the same spectral locations,[S12] which is in agreement with a tellurium evaporation mechanism. Tellurium evaporation and oxidation are both candidates for the decrease in the $MoTe_2$ Raman signal. The time dependent decrease in the Raman signal is plotted in Figure S4 c,d for the $N = 4$ region in Figure 1 d as well as an additional $N = 4$ region. Each mode is

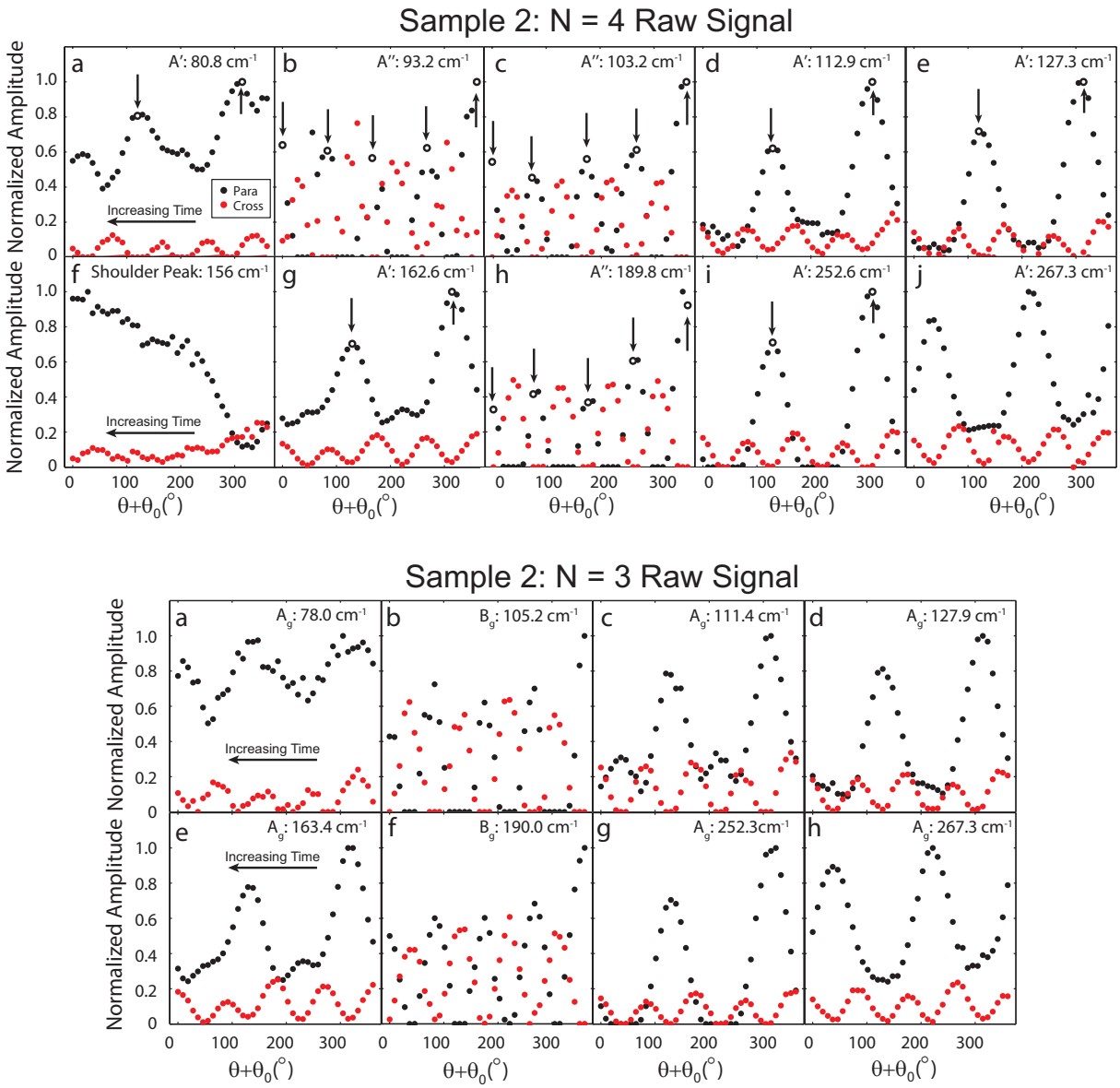

Figure S3: Raw normalized Raman amplitudes for parallel (red) and crossed (black) polarizations for the $N = 4$ and $N = 3$ region of Sample 2 from the main text. The symmetry and position for each mode are labeled. Signal decrease with time is attributed to laser damage.

normalized by its initial signal. The A_g/A' and B_g/A'' modes are shown in blue and red, respectively. These data were taken from the polarization dependence plots and therefore only the polarization angles that gave a maximum for each mode are shown. For these two different samples a similar signal decrease is observed and the empirical exponential fits are shown

as solid lines. Additional SHG images were taken afterwards and a decreased SHG signal in the damage area was observed. Figure S4 e shows an scanning electron microscopy (SEM) image of the sample in the main text and the laser damage sites are labeled. This shows that the $N = 4$ is still present, which suggests that the signal decrease is likely due to laser induced depletion of the tellurium.[S13,S14] Note that no laser damage from SHG measurements was observed. This suggests that there is either less absorption for lower energy photons or the damage is due to heating, which is more significant for continuous wave lasers. Regardless of the mechanism, great care is required when taking Raman spectra of this material.

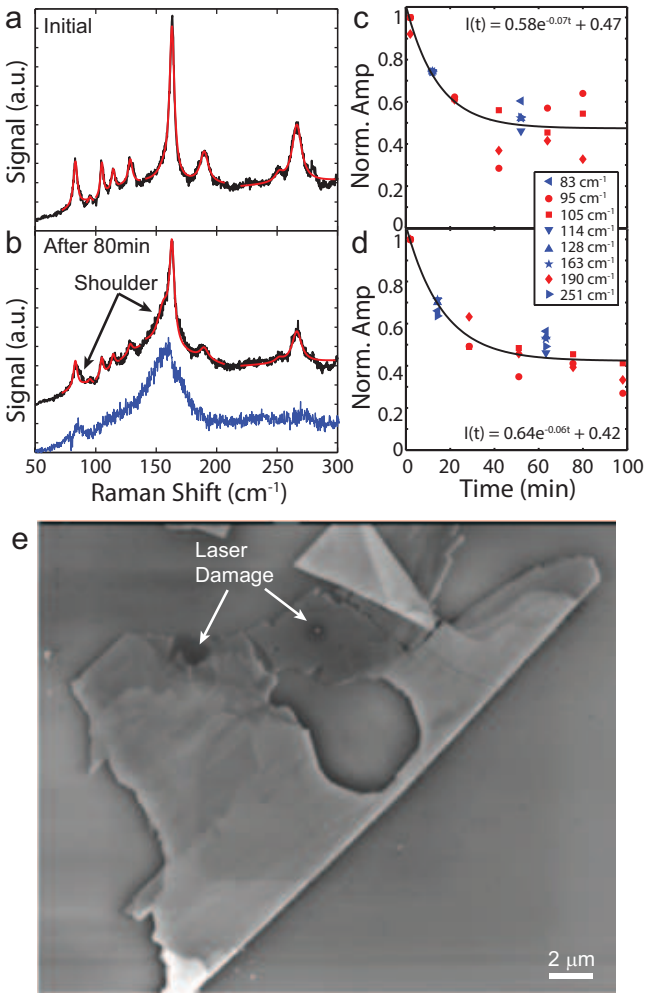

Figure S4: Raman spectra obtained during laser damage on $N = 4$ sample in Figure 1 d (a) initially and (b) after 80 min of laser exposure (black). Difference spectra of the initial and laser damaged spectra after scaling the amplitude is shown in blue to illustrate the shoulder peaks from the laser damage. (c),(d) Normalized amplitude of various Raman bands versus time for $N = 4$ sample in Figure 1 d and another $N = 4$ flake. (e) SEM image of sample in Figure 1 d after laser damage.

Sample orientation for SHG and Raman measurements

Figure S5(a),(b) shows the orientation of sample 2 on the SHG and Raman instrument, respectively. The dashed and solid white lines in Figure S5(a),(b) indicate the [010] crystal plane (y axis), respectively. This shows that there is a $\approx -10°$ angle difference in the sample mounting for the two measurements. Figure S5(c),(d) shows an SHG image and an optical image of sample 1 on the SHG and Raman instrument, respectively. The white

and black lines in Figure S5(a),(b) indicate the [100] crystal plane (x axis), respectively. This shows that there is a $\approx -16°$ angle difference in the sample mounting for the two measurements. The sample alignment for the two Raman images is almost identical with respect to the crystal axis, as expected from the polarized Raman measurements Figs. S2-S3.

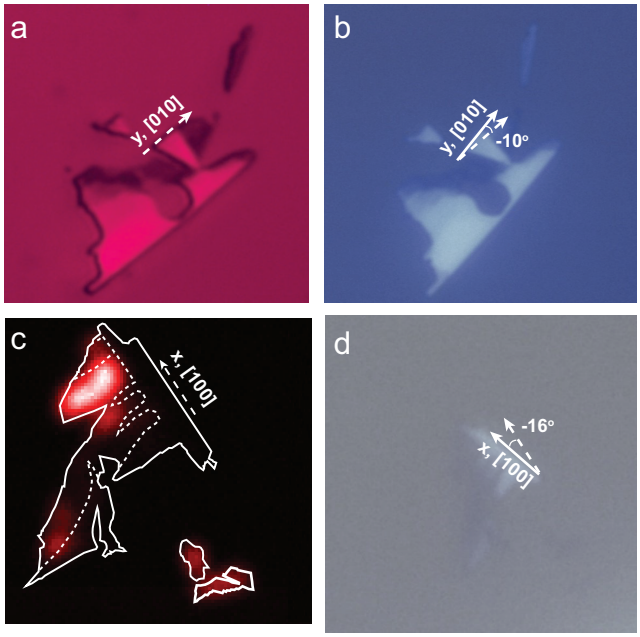

Figure S5: Optical image of sample 2 on the (a) SHG and (b) Raman instruments. The [010] crystal plane (y axis) is labeled in dashed and solid white lines, respectively. The angle difference in the sample mounting of $\approx -10°$ for the two measurements is indicated. (c) SHG and (d) optical images of sample 1. The [100] crystal plane (x axis) is labeled in dashed and solid white lines, respectively. The angle difference in the sample mounting of $\approx -16°$ for the two measurements is indicated.

Thickness verification using white light and Raman spectra

The thickness of the samples was verified using white light contrast and Raman spectra. The white light image of sample 1 from the main manuscript is shown in Figure S6 a. Linecuts along the 3L (red dashed line) and 4L (blue dashed line) for the blue, green, and red channels

of the camera are shown in Figure S6 b-d, respectively. The contrast was normalized using $(I - I_0)/I_0$. These cross sections show that contrast is better using green and red channels. The normalized contrast for the 4L region in the red and green channel is -0.4 and -0.3 in the green channel for the 3L region. The green channel indicates that the contrast is 33% higher for the 4L region in agreement with the AFM thickness measurements.

The thickness was also characterized using the Raman spectra. Figure S6 e shows the spectra of the $\approx$160 $cm^{-}1$ peak from the 3L (black) and 4L (red) regions. Generally the Raman signal scales with the volume of the sample. For two-dimensional materials, this means that the Raman signal should scale linearly with the number of layers. The ratio of the amplitudes and areas are 0.75 and 0.80, respectively, which is in good agreement with the AFM thickness assignments.

White light contrast for sample 2 are shown in Figure S7 a and the linecuts along the 4L (yellow line), 5L region (red line), and 6L (black line) are shown in Figure S7 b-d, respectively for the red and green camera channels. The laser damage from the Raman measurements is also labeled. The red channel for the 6L region does not have as much contrast as expected, which is likely due to the small size of the flake.

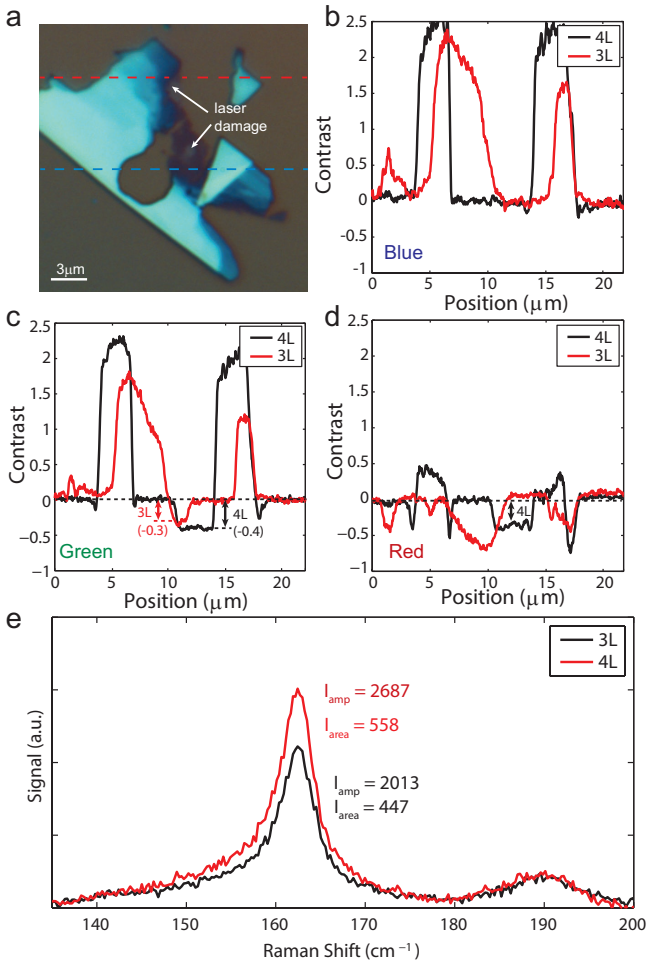

Figure S6: Sample thickness using white light contrast and Raman scattering (a) White light image of the flake taken using an RGB camera. The linecuts across the 3L (dashed red) and 4L (dashed blue) regions are shown. Linecuts from the (b) Blue, (c) green, and (d) red channels from the RGB camera with the 3L and 4L regions indicated. (e) Raman spectra of the $\approx$160 cm^{-}1 peak for the 3L and 4L regions. The area and amplitudes are labeled.

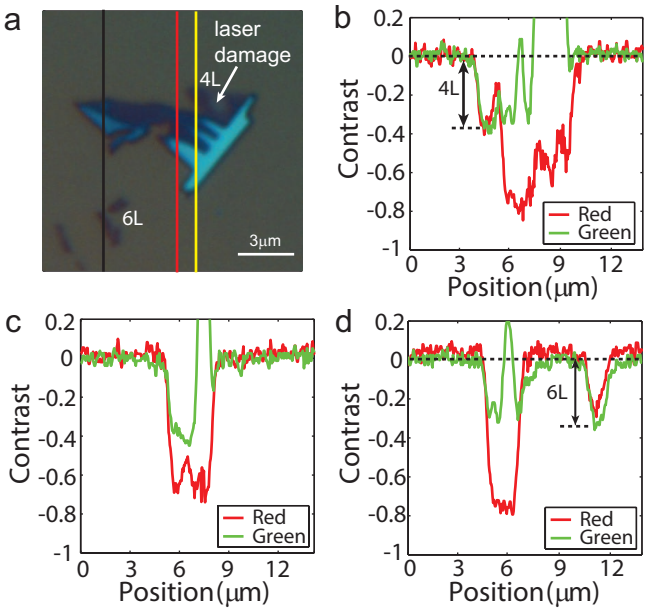

Figure S7: Sample thickness using white light contrast. (a) White light image of the flake taken using an RGB camera. The linecuts across the (b) 4L (yellow line), (c) 5L (red line), (d) 6L (black line) regions are shown. The green and red camera channels are shown.

SHG from additional flakes

Figure S8 show SHG measurements for four additional flakes with the thicknesses determined by AFM, white light, or both. The first column shows the SHG images with the topographic outlines and step edges shown as white lines. Figure S8 d-f shows a large 3L region with no SHG signal, whereas Figure S8 g-i shows strong SHG from the 4L region and the SHG image is in good agreement with the shape of the region from the white light region. Finally Figure S8 j-l shows a flake with a large number of step edges and the SHG image is again in good agreement with the step edges. These images provide additional evidence for the SHG only being present on thin even layer flakes.

Figure S9 shows the white light, topographic, and SHG images of the 10L crystal shown in green in Figure 4 f of the main text. The black square in Figure S9 a indicates the SHG scan area for Figure S9 c. Figure S9 b shows the topography with the 10L region near the bottom of the image.

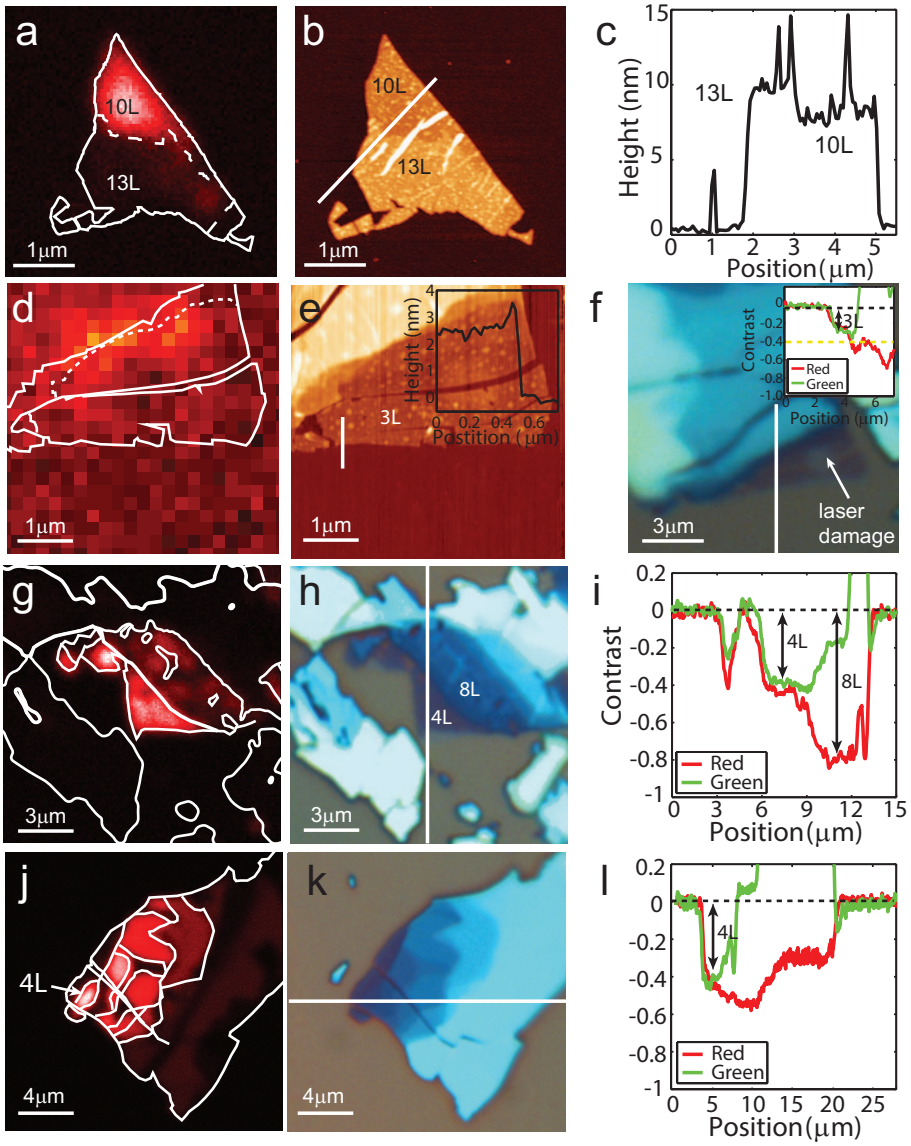

Figure S8: SHG images of additional flakes. First column shows the SHG images. The other two columns show AFM and white light images with linecuts to show the thicknesses. The red (red lines) and green (green lines) channels from the white light camera are shown.

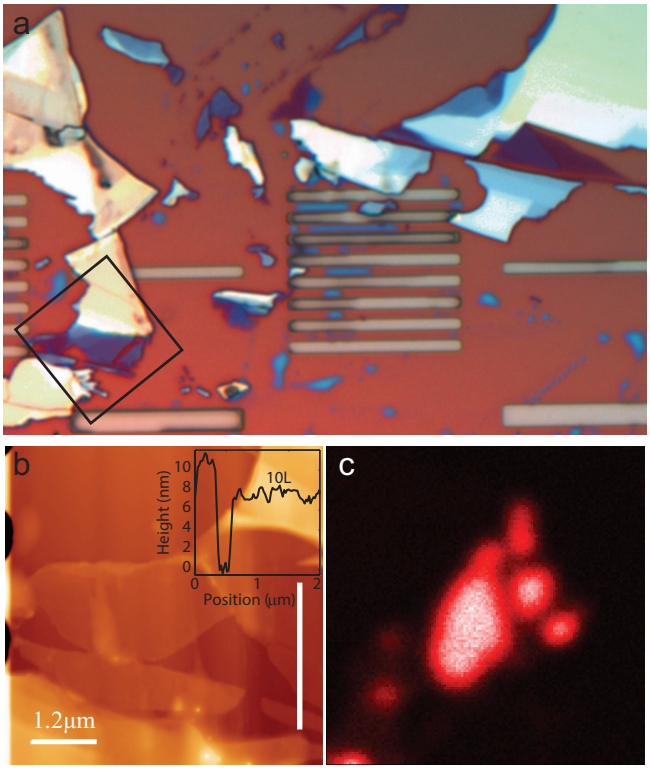

Figure S9: Images of the 10L crystal whose SHG polarization is shown in green in Figure 4f of the main text. (a) White light image and the black square shows the SHG scan window. (b) Topography image with part of the 10L region shown near the bottom. (c) SHG image of the 10L region.

Topographic images

Figure S10 shows the AFM images for Figure 4 of the main text.

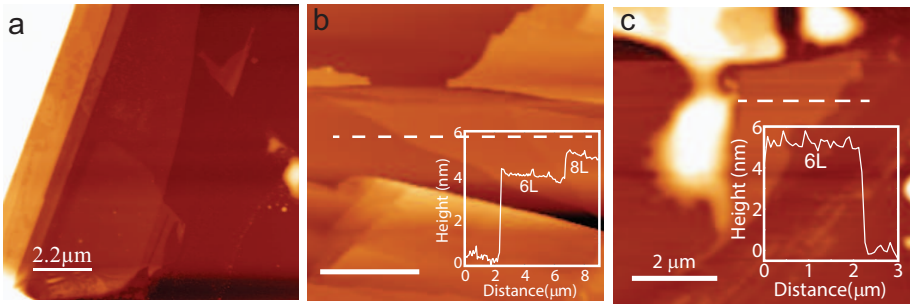

Figure S10: Topography of the regions in Figure 4 of the main text.

References

(S1) Dresselhaus, M.; Dresselhaus, G.; Jorio, A. *Group Theory: Application to the Physics of Condensed Matter*; SpringerLink: Springer e-Books; Springer Berlin Heidelberg, 2007.

(S2) Janisch, C.; Wang, Y.; Ma, D.; Mehta, N.; Elías, A. L.; Perea-López, N.; Terrones, M.; Crespi, V.; Liu, Z. Extraordinary Second Harmonic Generation in Tungsten Disulfide Monolayers. *Sci. Rep.* **2014**, *4* .

(S3) Ribeiro-Soares, J.; Janisch, C.; Liu, Z.; Elías, A.; Dresselhaus, M.; Terrones, M.; Cançado, L.; Jorio, A. Second Harmonic Generation in WSe_2. *2D Mater.* **2015**, *2*, 045015.

(S4) Kudryavtsev, A.; Lavrov, S.; Shestakova, A.; Kulyuk, L.; Mishina, E. Second Harmonic Generation in Nanoscale Films of Transition Metal Dichalcogenide: Accounting for Multipath Interference. *AIP Adv.* **2016**, *6*, 095306.

(S5) Mouri, S.; Miyauchi, Y.; Matsuda, K. Tunable Photoluminescence of Monolayer MoS_2 via Chemical Doping. *Nano Lett.* **2013**, *13*, 5944–5948.

(S6) Li, H.; Zhang, Q.; Yap, C. C. R.; Tay, B. K.; Edwin, T. H. T.; Olivier, A.; Baillargeat, D. From Bulk to Monolayer MoS_2: Evolution of Raman Scattering. *Adv. Funct. Mater.* **2012**, *22*, 1385–1390.

(S7) Chen, B.; Sahin, H.; Suslu, A.; Ding, L.; Bertoni, M. I.; Peeters, F.; Tongay, S. Environmental Changes in MoTe2 Excitonic Dynamics by Defects-Activated Molecular Interaction. *ACS Nano* **2015**, *9*, 5326–5332.

(S8) Cho, S.; Kim, S.; Kim, J. H.; Zhao, J.; Seok, J.; Keum, D. H.; Baik, J.; Choe, D.-H.; Chang, K.; Suenaga, K.; Kim, S. W.; Lee, Y. H.; Yang, H. Phase Patterning for Ohmic Homojunction Contact in $MoTe_2$. *Science* **2015**, *349*, 625–628.

(S9) Mirgorodsky, A.; Merle-Méjean, T.; Champarnaud, J.-C.; Thomas, P.; Frit, B. Dynamics and Structure of TeO_2 Polymorphs: Model Treatment of Paratellurite and Tellurite; Raman Scattering Evidence for New γ-and δ-Phases. *J. Phys. Chem. Solids* **2000**, *61*, 501–509.

(S10) Kumari, L.; Ma, Y.-R.; Tsai, C.-C.; Lin, Y.-W.; Wu, S. Y.; Cheng, K.-W.; Liou, Y. X-Ray Diffraction and Raman Scattering Studies on Large-Area Array and Nanobranched Structure of 1D MoO_2 Nanorods. *Nanotechnology* **2007**, *18*, 115717.

(S11) Camacho-López, M.; Escobar-Alarcón, L.; Picquart, M.; Arroyo, R.; Córdoba, G.; Haro-Poniatowski, E. Micro-Raman Study of the m-MoO_2 to α-MoO_3 Transformation Induced by CW-Laser Irradiation. *Opt. Mater.* **2011**, *33*, 480–484.

(S12) Amirtharaj, P.; Pollak, F. H. Raman Scattering Study of the Properties and Removal of Excess Te on CdTe Surfaces. *Appl. Phys. Lett.* **1984**, *45*, 789–791.

(S13) Clarke, R.; Marseglia, E.; Hughes, H. A Low-Temperature Structural Phase Transition in β-$MoTe_2$. *Philos. Mag. B* **1978**, *38*, 121–126.

(S14) Song, S.; Keum, D. H.; Cho, S.; Perello, D.; Kim, Y.; Lee, Y. H. Room Temperature Semiconductor–Metal Transition of $MoTe_2$ Thin Films Engineered by Strain. *Nano Lett.* **2015**, *16*, 188–193.